CO2 Electrolysis via Surface-Engineering Electrografted Pyridines on Silver Catalysts

Thomas Burdyny (t.e.burdyny@tudelft.nl)
Delft University of Technology https://orcid.org/0000-0001-8057-9558
Maryam Abdinejad
Delft University of Technology https://orcid.org/0000-0002-9279-3815
Erdem Irtem
Delft University of Technology
Amirhossein Farzi
McGill University https://orcid.org/0000-0003-4414-4033
Mark Sassenburg
Delft University of Technology
Siddhartha Subramanian
Delft University of Technology
Hugo-Pieter Iglesias van Montfort
Delft University of Technology
Davide Ripepi
Delft University of Technology
Mengran Li
Delft University of Technology https://orcid.org/0000-0001-7858-0533
Joost Middelkoop
Delft University of Technology
Ali Seifitokaldani
McGill University https://orcid.org/0000-0002-7169-1537

Article

Keywords:

Posted Date: January 25th, 2022

DOI: https://doi.org/10.21203/rs.3.rs-1274022/v1

CO_2 Electrolysis via Surface-Engineering Electrografted Pyridines on Silver Catalysts

Maryam Abdinejad,[a] Erdem Irtem,[a] Amirhossein Farzi,[b] Mark Sassenburg,[a] Siddhartha Subramanian,[a] Hugo-Pieter Iglesias van Montfort,[a] Davide Ripepi,[a] Mengran Li,[a] Joost Middelkoop,[a] Ali Seifitokaldani*[b] and Thomas Burdyny*[a]

a) Department of Chemical Engineering, Delft University of Technology, Van der Maasweg 9 2629 HZ Delft, the Netherlands

b) Department of Chemical Engineering, McGill University, Montreal H3A 0C5, Canada

Corresponding author

Ali Seifitokaldani*[b] and Thomas Burdyny*[a]

Abstract

The electrochemical reduction of carbon dioxide (CO_2) to value-added materials has received considerable attention. Both bulk transition metal catalysts, and molecular catalysts affixed to conductive non-catalytic solid supports, represents a promising approach towards electroreduction of CO_2. Here, we report a combined silver (Ag) and pyridine catalyst through a green and irreversible electrografting process, which demonstrates enhanced CO_2 conversion versus the individual counterparts. We find by tailoring the pyridine carbon chain length, a 200 mV shift in the onset potential is obtainable compared to the bare silver electrode. A 10-fold activity enhancement at -0.7 V *vs* RHE is then observed with demonstratable higher partial current densities for CO indicating a co-catalytic effect is attainable through the integration of the two different catalytic structures. We extended performance to a flow cell operating at 150 mA/cm^2, demonstrating the approach's potential for substantial adaption with various transition metals as supports, and electrografted molecular co-catalysts.

Introduction

Carbon dioxide (CO_2) is a primary contributor to global climate change.[1] Capture and electrochemical CO_2 reduction reaction (CO_2RR) to value-added feedstocks and chemicals offer a promising approach to sustainable energy storage that leverages renewable sources.[2,3] Despite its abundancy, the CO_2 molecule is thermodynamically stable, making its electroconversion challenging in terms of: (i) competition with the hydrogen evolution reaction (HER) in aqueous environment, ii) low stability, and iii) high overpotentials.[3]

To subvert activity and selectivity challenges for CO_2 reduction, researchers have developed numerous classes of catalysts. Two classes frequently used and modified are: bulk transition metals,[4] and molecular catalysts[5,6]. Both seek to activate the linear CO_2 molecule towards a desired product at enhanced reaction rates, while simultaneously limiting the electrochemical activity of the competing HER. Commonly-utilized bulk transition metal catalysts are silver and copper, with common catalytic modifications to enhance performance occurring as a result of varying bulk morphology and surface area.[7–9] Alternatively, molecular catalysts range broadly from single-metal sites such as porphyrin and phthalocyanines,[10,11] to metal-free complexes (e.g. pyridine),[5] with modifications accessible by varying chain lengths, metal sites, and supporting ring structures. For these systems, the interactions between aqueous CO_2 and the molecular catalyst's ligands can act as a capturing site for CO_2, while the designed center sites can provide the conversion step. Through characterizations and modifications both catalytic approaches are separately able to near-unity selectivity towards CO at elevated current densities, with improved efficiency and stability, which represent the key performance targets for CO_2RR.

While both bulk transition metal surfaces and molecular catalysts individually represent viable options for CO_2 conversion, many of the modifications available to further increase activity and decrease activation potentials have been well-explored, providing diminishing returns on performance metrics. Alternatively, affixing a CO_2RR active molecular catalyst onto a CO_2RR active catalytic support approaches may provide performance enhancements beyond the individual catalysts themselves by allowing for dual-functionalities that overcome individual limitations. Flexibility in further modifying the collective system is then also

provided. Emerging approaches to hybrid systems then have the potential to combine the two best catalyst traits of the individual systems: localizing the CO_2 capture ability of molecular catalysts near an electrode's surface followed by utilizing the large active area, and conversion of a bulk transition metal.[5,12–14]

Here, we sought to investigate the potential for CO_2-reactive molecular catalysts to be affixed to a CO_2-reactive support. Such a demonstration would open a new parameter space of combined catalysts to explore. A challenging aspect of a combined approach is affixing a molecular catalyst close enough to a transition metal catalyst so that they do not function independently. Without this, no advantage can reasonably be expected over the separate cases.

From these inclinations, we hypothesized that integration of an N-based molecular catalyst traditionally used in homogeneous environments would pair well with a heterogeneous silver electrocatalyst for a number of reasons. Firstly, N-based molecular catalysts such as pyridine complexes provide a CO_2-capture effect,[15] and have demonstrated but poor electroreduction of CO_2 in homogeneous environments, albeit at low rates and selectivity.[16–20] Second, pyridine can be modified with variable chain lengths which, if affixed to a heterogeneous support, as it allows for the distance between the electrode surface and the CO_2 capture site of the pyridine ring to be controlled and tuned. To ensure a bond between the ligand of the pyridine molecular catalyst and the silver support that can withstand a reducing potential, the novel field of electrografting shows promise.[21,22]

Here the immobilization of pyridine derivatives onto Ag nanoparticles was demonstrated using a molecular electrografting technique that incorporates diazonium chemistry, enabling green and irreversible fixation onto the electrode surface, resulting in reduced overpotentials versus the individual catalysts. We investigate the CO_2RR performance for a variety of hybrid molecular/nanoparticle catalysts, showing how the distance between the pyridine capture site and the electrode surface impacts overall catalytic efficiency. To examine the propensity for a combined transition metal and molecular catalyst to work in unison, we designed a set of experiments to test both homogeneous and heterogeneous catalytic systems (Figure 1). Namely we tested the activity and selectivity for CO_2 electroreduction in four control cases: using a carbon and silver electrode

with pyridine present only in the electrolyte (Case 1 and 2, respectively), pyridine electrografted to carbon electrode (Case 3 – EPy), and pyridine electrografted to a silver electrode (Case 4 – Ag-EPy). Before we could make these comparisons, however, we first needed to confirm that it was indeed possible to irreversibly affix pyridine complexes to silver catalyst.

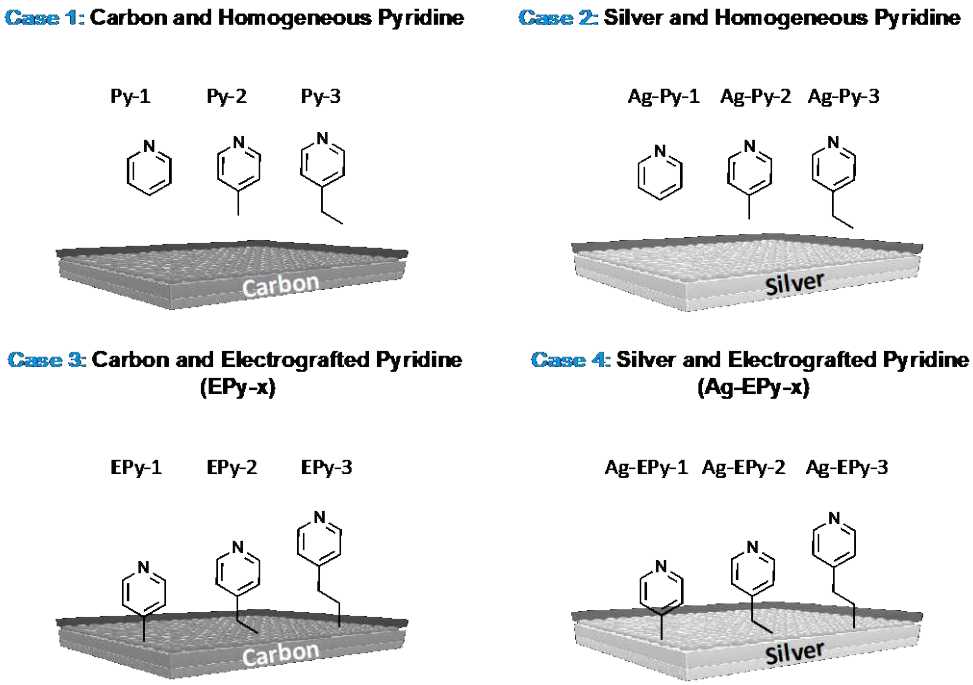

Figure 1. Schematic of: **Case 1.** Homogeneous pyridine molecular catalysts with glassy carbon carbon electrode (Py-1, Py-2, and Py-3); **Case 2.** Homogeneous pyridine molecular catalysts with slilver electrode catalysts (Ag-Py-1, Ag-Py-2, and Ag-Py-3); **Case 3.** Heterogeneous electrografted pyridine catalysts onto glassy carbon electrode (EPy-1, EPy-2, EPy-3); **Case 4.** Heterogeneous electrografted pyridine catalysts onto silver electrode (Ag-EPy-1, Ag-EPy-2, and Ag-EPy-3).

While all combined catalysts show increased activity, the 2-carbon chain length pyridine complex elicited a 200 mV decrease in onset potential at 1 mA cm^{-2}, and a 10-fold improvement versus bare Ag at a voltage of -0.7 V *vs* RHE. We provide attenuated total reflectance surface-enhanced infrared absorption spectroscopy (ATR-SEIRAS) measured and density Functional Theory (DFT) computations of the system to assess the production rates and mechanisms of the different catalysts. Finally, we demonstrate the

stability and efficiency of the electrografted system at elevated current densities through flow-cell experiments up to 200 mA cm^{-2}.

Results

Synthesis and Structural Characterizations of Electrografted Pyridines onto Electrode Surfaces

To begin the electrografting process in H-cells we first prepared the Ag electrode using electrodeposition of a 1 mM $AgNO_3$ solution with 0.1 M $KHCO_3$ at a constant applied potential of -0.2 V *vs* RHE for 200 s (Figure S1).[23] With the Ag surface ready, amino pyridine derivatives were then oxidized to diazonium cations through electrochemical reduction, and simultaneously electrografted onto an electrode surface *in situ* (Figure 2a).[22] In line with the motivation for controlling the distance between the pyridine ring and the Ag surface, we used pyridine complexes of 1-3 carbon chains, denoted as Ag-EPy-1, Ag-EPy-2 and Ag-EPy-3. Figure 2b and S2a depicts the electrografting of EPy-2, and Ag-EPy-2, where peak surface coverage was achieved after 3-5 cyclic voltammetry (CV) cycles. The highest catalytic activity was observed after 5 cycles. A characteristic irreversible reduction peak was used to identify the reduction of diazonium salt to form the aryl radical intermediate, promptly followed by the formation of a covalent bond to the electrode surface and release of N_2 gas.[24–27]

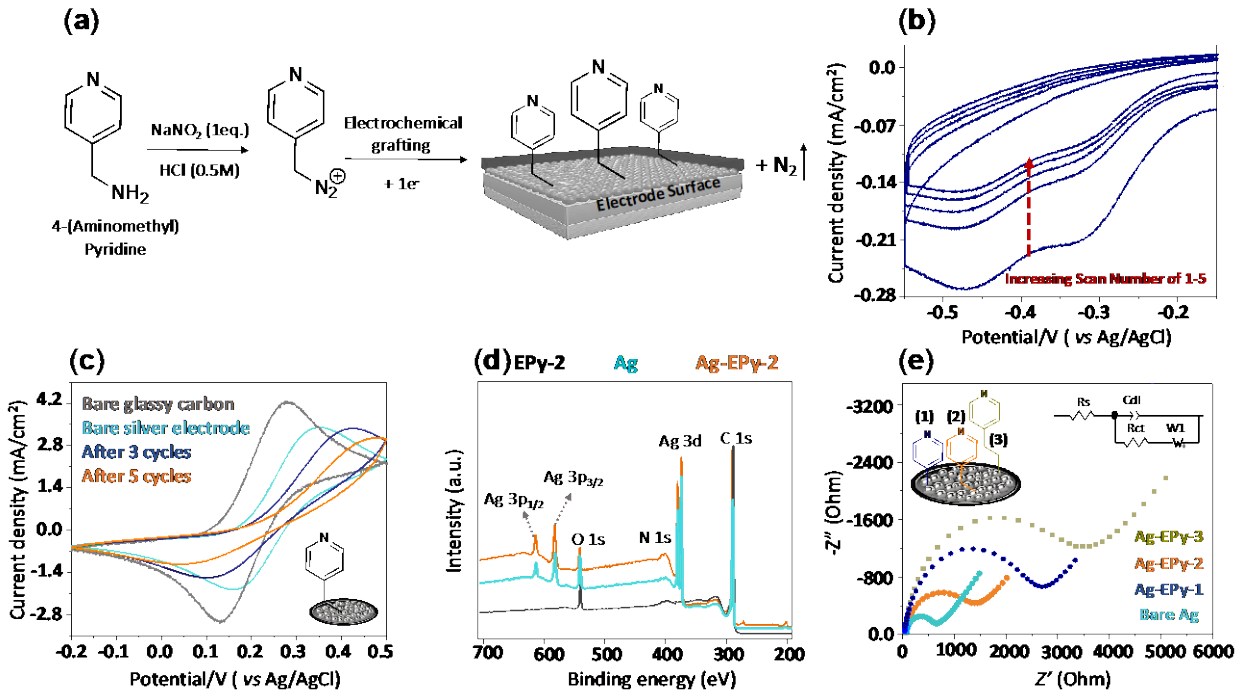

Figure 2. (a) Preparation of pyridine-diazonium cations generated *in situ* to form electrografted Ag-EPy-2; (b) Electrografting voltammogram of 5 mM of 4-(Aminomethyl) Pyridine onto silver electrode in 2 mM $NaNO_2$ and 0.5 M HCl at a scan rate of 50 mV/s; (c) Cyclic voltammetry (CV) comparison of a ferricyanide redox probe (2.5 mM $K_4Fe(CN)_6$/200 mM KNO_3 before and after electrografting at a scan rate of 50 mV/s; (d) X-ray photoelectron spectroscopy (XPS) survey spectra of Ag, EPy-2 and Ag-EPy-2; (e) Nyquist diagrams of bare glassy carbon, Ag, and Ag-EPy-1-3 in 2.5 mM $[Fe(CN)_6]^{3-/4-}$ and 200 mM KNO_3.

A CV study with a ferricyanide redox probe (aqueous 2.5 mM $K_4Fe(CN)_6$/200 mM KNO_3) better illustrates the successful formation of the organic layer on the electrode surface (Figure 2c and Figure S2b). A significant decrease in current density of the probe's redox profile was observed before and after molecular deposition, indicating that the access of the probe to the electrode is effectively obstructed due to the formation of the pyridine layer on the electrode surface.[28] To further confirm the presence of surface pyridine we performed a surface analysis with X-ray photoelectron spectroscopy (XPS) (Figure 2d).[29] Survey spectra of EPy-2, Ag-EPy-2, and bare Ag electrode find C 1s, N 1s, and O 1s peaks at 284, 399, and 530 eV, respectively. Peaks at 368, 573 and 604 eV correspond to Ag 3d, $3p_{3/2}$ and Ag $3p_{1/2}$, respectively.[30] The increase in the peak intensity of C 1s and N 1s was observed for the electrografted EPy-2 and Ag-EPy-

2 compared to that of bare Ag which could be due to the formation of pyridine layer onto the electrodes' surfaces.[31] No Ag 3p peaks were observed in the case of the homogeneous case (EPy-2) where pyridine was suspended in the electrolyte phase. These results are in agreement with similar reports.[32,33]

Lastly, to assess the charge transfer dynamics of the affixed pyridine at the electrode's surface versus bare carbon and silver, we used electrochemical impedance spectroscopy (EIS) in the 2.5 mM $[Fe(CN)_6]^{3-/4-}$ redox probe in 200 mM KNO_3 solution (Figure 2e and Figure S2c). The Nyquist plots pictured in Figure 2e ascribes the largest charge transfer with Ag-EPy-3 (3510.2 ± 72.1 Ω) followed by Ag-EPy-1 (2534.4 ± 50.3 Ω), Ag-EPy-2 (1492.6 ± 38.9 Ω), and bare Ag (690.7 ± 21.9 Ω), respectively. A significant increase in the resistance can be seen across all systems in the presence of the immobilized pyridine compounds.[34]

Electroreduction of CO_2 in H-Cell

With the combined silver nanoparticles and electrografted pyridine molecular catalyst formed, we now test the comparative CO_2 electrolysis performance of the varied chain lengths (Ag-EPy1-3), as well as the controlled systems. These were first performed in a two-compartment H-cell with a three-electrode configuration including an Ag/AgCl reference electrode and Pt counter electrode in a CO_2-saturated 0.1 M $KHCO_3$ aqueous solution (Figure 3a).[35]

The initial CV comparison of the heterogeneous systems (Cases 3 and 4) were carried out in the presence and absence of CO_2. The comparison highlights a substantial increase in current density upon saturation of the solution with CO_2 (Figure S3 and S4). The linear sweep voltammetry (LSV) of the immobilized pyridine-catalysts (EPys) onto glassy carbon electrode (GCE) see a CO_2 reduction onset potential arise at ~-0.8 V *vs* RHE (Figure 3b). Compared to that of the GCE control, the Ag-EPys electrode systems show a general increase in current density coupled with a noticeable positive shift to lower onset potential (~-0.6 V *vs* RHE), defined at 1 mA/cm (Figure 3c). A large overpotential is often attributed to the activation energy barrier of the initial electron transfer that forms the $CO_2^{\cdot-}$ intermediate, which is poorly stabilized by the silver and glassy carbon electrode surfaces.[36] It is evident that the immobilized pyridine molecules show a

clearly more positive onset potential compared to bare Ag, higlighiting the role of the affixed pyridine as a co-catalyst which improves the overall electrochemical activity as compared to the bare Ag electrode alone.

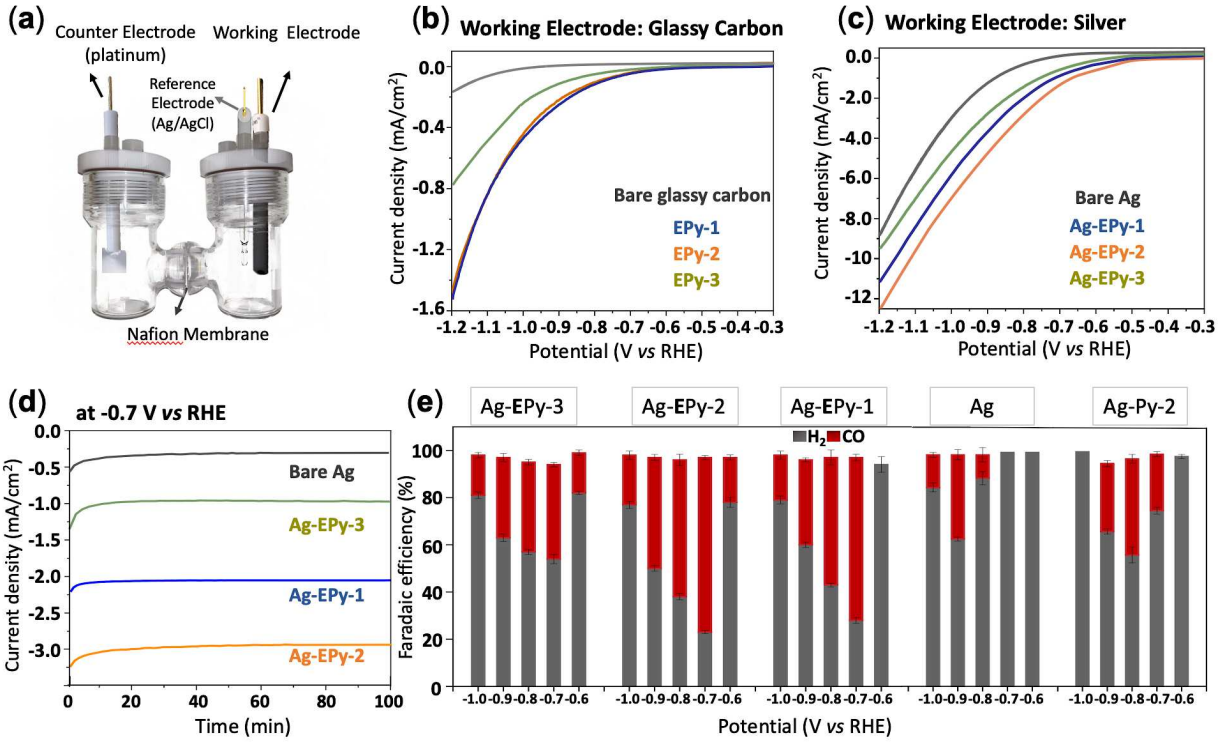

Figure 3. (a) Schematic for H-cell setup. Cyclic voltammetry (CV) comparison of heterogeneous pyridine electrocatalysts at (b) glassy carbon electrode (EPy-1-3); (c) silver electrode (Ag-EPy-1-3) under Ar and CO_2. (d) Chronoamperometry comparison of bare Ag and Ag-EPy-1-3 in 0.1 M $KHCO_3$ at -0.7 V *vs* RHE under CO_2. (e) Faradic efficiency (FE) comparison of Ag-EPy 1-3, Ag-GCE, bare Ag, and homogeneous Ag-Py-2 at -0.6, -0.7, -0.8, -0.9 and -1.0 V *vs* RHE in 0.1 M $KHCO_3$.

Electrolysis was then performed at fixed potentials to allow for the comparative activity and selectivity to be measured (Figure S5-S6). In all cases, H_2 and CO were the only gaseous products measured and formate was observed as the sole liquid product. The resulting chronoamperometry measurements at -0.7 V *vs* RHE in Figure 3d shows that the highest current density is observed for the 2-carbon electrografted sample (Ag-EPy-2), with a ~10-fold increase in current density over the bare Ag sample at the same potential. The increase in activity is also exhibited as improved selectivity towards CO as shown in Figure 3e, where the combined transition metal and molecular catalysts exhibited higher CO_2 to CO selectivity than both the heterogeneous Ag catalyst, and the homogeneous pyridine catalyst (Ag-

Py-2) over all potentials. These results not only highlight the advantages of the combined catalytic system (Case 4) versus the separate cases (Cases 1-3), but also the importance of the pyridine chain length. For example, Ag-EPy-2 showed the greatest catalytic activity in the heterogeneous media at -0.7 V *vs* RHE (Figure 3e), with the FE= 74% and j = -3.1 mA/cm^2 compared to Ag-EPy-1 (FE: 69%; j: -2.26 mA/cm^2) and Ag-EPy-3 (FE: 40%; j: -1.2 mA/cm^2).

For a systematic comparison, 5 mM of homogeneous pyridine catalysts Py-1-3 (Figure S9-Figure S17) in 0.1 M $KHCO_3$ was also applied over the same potential range of -0.5 to -1.0 V *vs* RHE. These homogeneous catalysts showed a low catalytic activity at a higher potential of ~-0.8 V *vs* RHE in comparison to the heterogeneous controls.

The above electrochemical experiments highlight the potential for increased activity and selectivity for the combined transition metal and molecular system. Next, we apply mechanistic studies to investigate the interactions between the Ag support, the electrografted pyridine and the CO_2 reduction reaction.

Mechanistic Study

We performed a number of mechanistic studies to determine the cause of the increased rate of electron transfer observed in the electrochemical experiments in the presents of pyridine complexes. These include CV sweeps under different scan rates, measurements of the Tafel slopes of different catalysts, a DFT analysis and surface spectrometry.

The difference in peak separation upon applying the CV scan rate can be used to quantify the heterogeneous electron transfer rate constant between the electrode and molecular catalyst species.[37] Therefore, to shed light on the increased rate of electron transfer between the electrode and the catalytic layer with different carbon chains, the detailed electroreduction of CO_2 in both EPys and Ag-EPys was evaluated at several scan rates of 100, 120, 160, 180, and 200 mV/s and reported in Figure S18. A linear relationship between the reduction peak currents and the square root of the scan rate ($v^{1/2}$) was observed, suggesting that the rate of CO_2 reduction is dictated by its rate of diffusion.[38] As shown in Figure S19, the slope of the catalyst 2 is

larger than that of 1 and 3 in both GCE and Ag electrode surfaces indicating a higher electron transfer hence having a better electrochemical activity for CO_2RR. This phenomenon should result in higher electrochemically active surface area (ECSA) of 2 compared to 1 and 3. Taking into account the experimentally determined slopes were applied[39,40] and ECSA of GCE (0.071 cm^2) EPy-1 (0.074 cm^2), EPy-2 (0.074 cm^2), EPy-3 (0.073 cm^2), and Ag-EPy-1 (0.078 cm^2), Ag-EPy-2 (0.099 cm^2), Ag-EPy-3 (0.073 cm^2), Ag (0.092 cm^2) was calculated accordingly. Comparing the results, the higher ECSA of 2 in both cases of GCE and Ag electrodes, again confirms the highest catalytic performance of the 2 among the others which could be due to its better synergistic interaction with electrode, higher electron transfer, and larger surface area.

Next, to obtain additional insight on the reaction kinetics of the best catalyst, Tafel slopes of Ag-EPys were calculated in 0.1 M $KHCO_3$ for the electrochemical CO_2RR (Figure S20). The slopes are 124.2, 120.6, and 152.2 mV/dec, for Ag-EPys 1-3 respectively. The smallest Tafel slope value belongs to Ag-EPy-2 confirming the faster reaction kinetics are influenced by better electron transfer between the molecular catalyst and silver electrode surface.[41] Similar behavior has been observed previously using N-based compounds.[42–44]

DFT calculations were performed to gain further insight into the increased CO_2RR activity of the deposited pyridine catalysts with the silver electrode (Ag-EPys) (Figure S21-S24). The role of the pyridine group and that of the length of the carbon chains in facilitating the electron transfer towards the improvement of the CO_2RR catalytic performance are observed through calculating the reaction energy diagram and charge delocalization. CO_2RR to CO is studied through 2 proton-coupled-electron-transfer (PCET) steps[45] and via carboxyl intermediate formation. As depicted in Figure 4a and Table S1-S2, the Ag-EPy-2 demonstrates the lowest energy barrier compared to the other two Ag-EPys. This reaction energy diagram reveals that the adsorption of *COOH is the rate determining step, where different Ag-EPys demonstrate different energy barrier for this step through the following order: Ag-EPy-2 (779 meV) < Ag-EPy-1 (784 meV) < bare Ag

(804 meV) < Ag-EPy-3 (828 meV). This order is consistent with experimental observation of the overpotentials (Table S3).

To further investigate the role of pyridines in this elementary step, charge delocalization around N-group of the pyridines and active Ag sites are demonstrated in Figure 4b and Figure S25-26. The Bader charge analysis is performed to quantify the charge that is transferred during the reaction. According to Figure S27, *COOH is adsorbed in a top-site configuration (e.g., Ag2 in Figure 4b, with adjacent Ag1 and Ag3 atoms). Results of the Bader charge analysis and charges attributed to each Ag atom, before and after the *COOH adsorption, reveal that the largest charge donation occurs with Ag-EPy-2 (0.1783 e^-) followed by Ag-EPy-1 (0.1755 e^-) and Ag-EPy-3 (0.1671 e^-), respectively (Table S4). The largest contribution comes from the central Ag site (Ag 2) in all three cases which is anticipated because of its shorter distance from the adsorbate. Two oxygen atoms within the adsorbed carboxyl intermediate change the electron density around Ag1 and Ag3. However, the oxygen above the Ag3 is bonded to the hydrogen, lowering its electronegativity compared to the other oxygen atom above the Ag1, thereby Ag1 donates more charges than Ag3.

The reaction pathways for electroreduction of CO_2 to CO and formate using the Ag-EPy-2 electrode were further studied using *in situ* ATR-SEIRAS (Figure S28-S30), which aids in characterizing the catalytic active sites experimentally.[46,47] The measurements were performed in a customized, spectroelectrochemical H-cell which housed the Ag-EPy-2 working electrode, a Ag/AgCl reference electrode, and a graphite counter electrode (Figure 4c). CO_2RR was first studied on bare silver (Figure S30), then with Ag-EPy-2 (Figure 4d-4e) at increasing potentials from -0.5 to -1.9 V *vs* Ag/AgCl in 0.1M $KHCO_3$ saturated with CO_2.

Recording the evolution of the ATR spectra over time at various potentials under CO_2 flushing, we can get insight on the reaction mechanism and product intermediates. As shown in Figure 4d and 4e, after several minutes of electrolysis, the *CO band arises at ~1980 cm^{-1}. Concurrently, the O-H broad band of weakly hydrogen-bonded interfacial water molecules trends inversely above 3000 cm^{-1}. Two large peaks at 1288 cm^{-1} and 1389 cm^{-1} correspond to the C–OH and a symmetric stretch of COO^-.[48,49] The peak at 1670 cm^{-1} belongs to a combination of the H–O–H bend and C═O asymmetric stretch which is assigned to the

COOH/COO^- intermediates, which is in agreement with previous reports.[50] Additional bands situated between 1000 and 1450 cm^{-1} correspond to interfacial carbonates and bicarbonates and show similar trends in both cases, pointing to comparable surface pH values.[51] The peak around 1580 cm^{-1} attributed to PyH^+ is absent in the case of bare Ag (Figure S30). The increase in the intensity of CO_2 consumption at ~2400 cm^{-1} shows that CO_2 is consumed at a [3:2] ratio for [Ag-EPy-2: bare Ag]. The initial shift to higher wavenumber in the CO_2 peak may be attributed to the increasing coverage of CO_2 on pyridine modified surfaces, whereas the same shift is negligible in the case of bare-Ag.[52] Based on previous reports,[15,53,54] and our findings, we hypothesize both silver and -N groups of pyridine molecules act as a dual active site towards CO_2RR, thus increasing the concentration of CO_2 on the electrode surface, responsible for a superior catalytic performance.

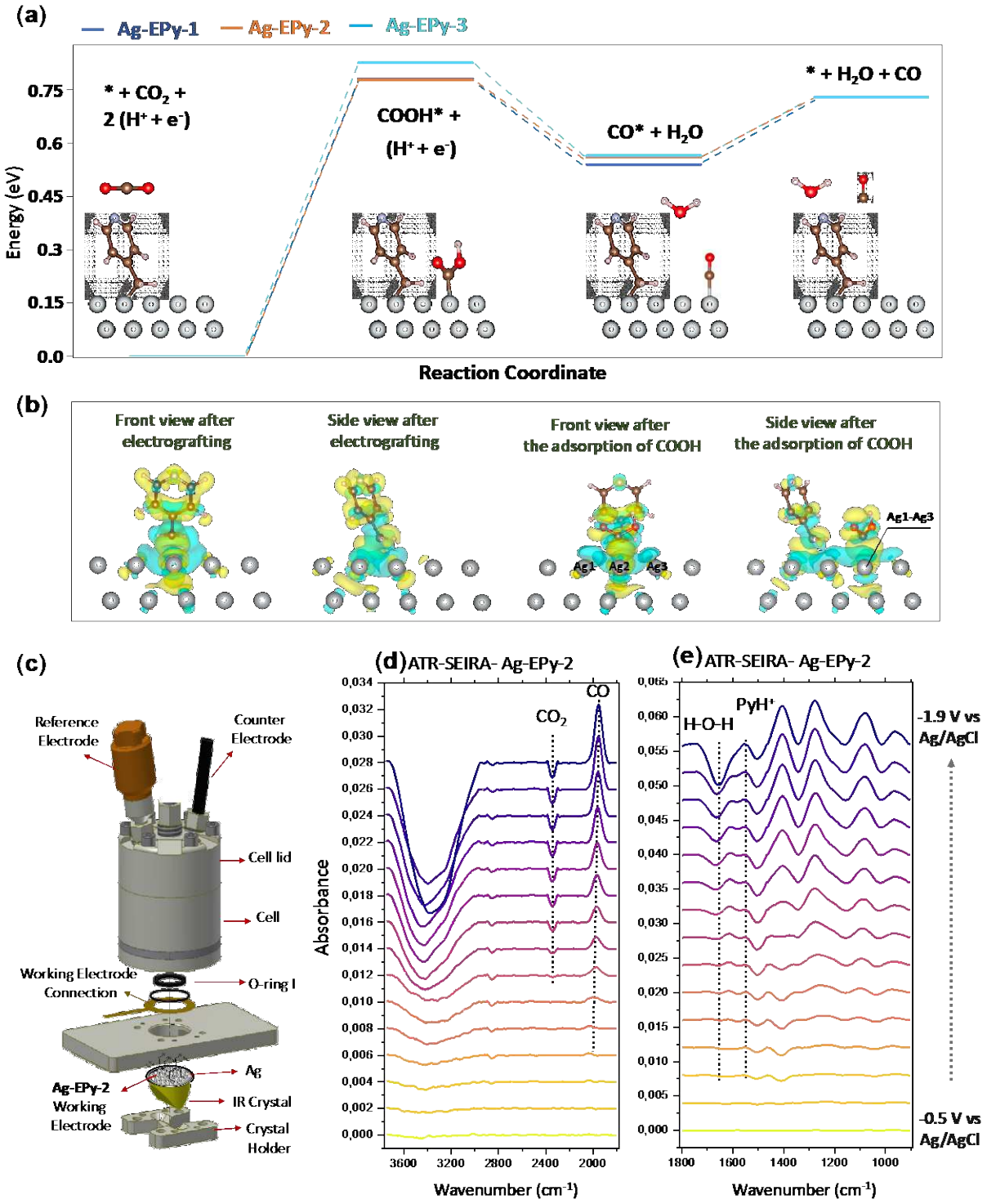

Figure 4. (a) Reaction energy *vs* reaction coordinate (Schematics shown for Ag-EPy-2). (b) Deviations in charge densities after electrografting Ag-EPy-2 from different views before and after of *COOH adsorption. (c) Schematic for the customized attenuated total reflectance attenuated total reflectance surface-enhanced infrared absorption

spectroscopy (ATR-SEIRAS); (d,e) ATR-SEIRA transmission spectra of immobilized Ag-EPy-2 at different potentials in 0.1 M $KHCO_3$ electrolyte under CO_2.

With the experimental demonstration of the combined catalytic system resulting in improved electrochemical performance, and potential mechanisms investigated, we aimed to apply the combined system in flow cell operation to reach higher current densities.

Electrografting of Pyridines onto gas diffusion electrodes and electroreduction of CO_2 in flow cells

Although H-cells are useful for exploring material combinations and mechanistic studies with fine control, the performance of catalysts within H-cell aqueous systems for CO_2 reduction is limited by the low solubility of CO_2 in aqueous solution and accessibility of active sites.[55,56] For elevated reaction rates due to improved mass transport and higher surface areas, researchers have turned to flow cell systems which may use a gas-diffusion electrode to support catalytic structures.[44,49–53] Here we sought to demonstrate the implementation of the Ag-EPy system onto a gas-diffusion layer and in different flow cells to prove both the catalytic stability of the system, and demonstrate the potential for two catalytic systems to be combined in this setup.

To this end, we chose the best catalyst, Ag-EPy-2 to be translated from the H-cell to zero-gap membrane electrode assembly (MEA). The MEA cell consists of an anode chamber with a liquid phase anolyte and a cathode chamber with a gas phase inlet (Figure 5a, Figure S31-S32).[61,62] In this design, humidified CO_2 is delivered directly to the active materials through a serpentine flow channel located at the back side of the gas diffusion electrode (GDE). For the flow cell configuration (Fig S34) the catholyte solution was circulated between the GDE and the membrane.

The GDE was prepared by sputtering 10 nm Ag onto the gas diffusion layer (GDL) to form a hydrophobic and microporous layer. Next, Py-2 was successfully electrografted onto the Ag using a technique identical to the one described above to form Ag-EPy-2 (Figure S33). The electrografting was conducted with 3, 5

and 10 cycles to determine the best surface coverage with pyridines for the CO_2RR, and ensure the pyridine fully coated the now 3-D porous electrode structure. Similar in H-cell, the 5 cycles demonstrated the best catalytic activity, while after 5 cycles the electrode conductivity decreased. Immobilized Ag-EPy-2 on a GDE was then used as a working electrode with a nickel counter electrode as the anode, both with a surface area of 6 cm^2. To the best of our knowledge, it's a first report on molecular electrografting immobilization on GDE.

The catalytic activity of Ag and Ag-EPy-2 was subsequently investigated at current densities ranging from 25 to 200 mA/cm^2 (Figure 5b). To determine the cell potential at each current density, currents were applied stepwise (Figure 5c). Comparing Ag, EPy-2, and Ag-EPy-2 finds a lower cell potential when Ag-EPy-2 is used, highlighting the importance of having both Ag and pyridine in combination for enhancing overall catalytic performance which has been hypothesized in this work. The pyridine complex also showed high CO selectivities, on par to that of pure Ag in an MEA configuration, with slightly lower observed HER which may be attributable to the reduced operating voltages and earlier onset potential of CO versus bare Ag (Figure 5d). The reduction in applied potential then indicates that the complex, and the approach in general, can show CO_2RR advantages even when selectivity of the base system is high.

To further study the role of electrografted pyridine in improving the silver electrode surface stability, similar experiments were performed using a flowing catholyte system rather than the above MEA configuration (Figure S35).[63] Here the overall selectivity towards CO was lower, but was maintained at higher overall current densities. Further optimization of these systems may then be needed to avoid HER.

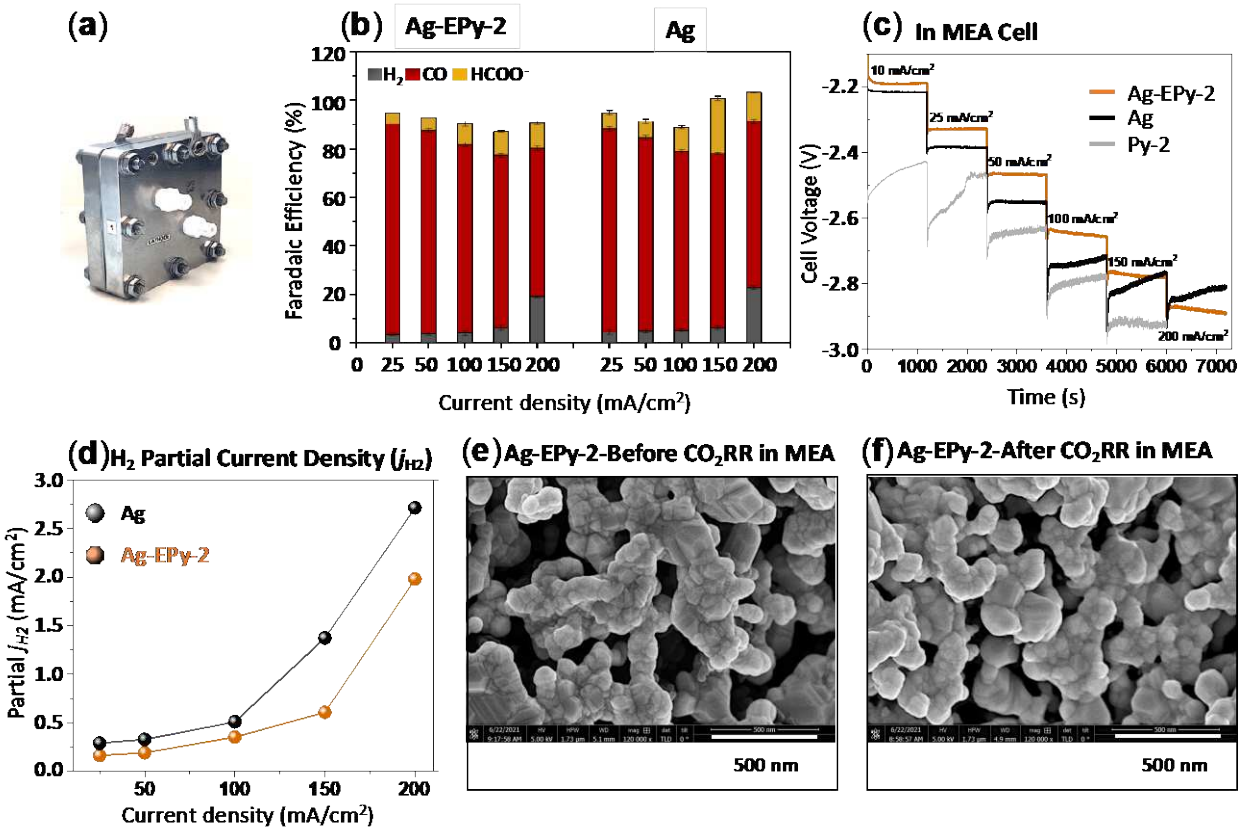

289

290 **Figure 5.** (a) Membrane electrode assembly (MEA) cell for the electrochemical reduction of CO_2; (b) Faradaic
291 efficiency (FE) comparison of Ag and Ag-EPy-2 at current densities of at 25, 50, 100, 150 and 200 mA/cm^2 in a MEA;
292 (c) sketch graph of voltage against time at different current steps in the range of 25-200 mA/cm^2; (d) Partial current
293 density comparison of hydrogen (j_{H2}) using Ag and Ag-EPy-2 for CO_2 electroreduction; Scanning electron microscopy
294 (SEM) of Ag-EPy-2 (e) before; and (f) after electrochemical CO_2RR.

295 Finally, we performed scanning electron microscopy (SEM) to visualize the surface morphology and
296 document any morphological stability changes during the CO_2RR of the Ag-EPy system. Comparison of
297 SEM before and after 2 hours CO_2 electrolysis in the flow cell finds no significant variations in surface
298 morphology, attesting to the high stability of the catalysts to the local environment imposed at high current
299 density (Figure 5e-f, and Figure S37). This is further confirmed with atomic force microscopy (AFM)
300 studies (Figure S38-S39). These studies including height sensor images, peak force error images, and 3D
301 topographies, show no discernable change of catalyst microstructure during the high-electrolysis process.

Discussion

Herein, we report a new approach to improve CO_2RR through the design of a hybrid molecule/support structure. The approach taken in this work is built on the synergistic effect of pyridine groups with an Ag surface, which was carefully investigated by altering the alkyl chain length of several pyridine derivations. In successfully electrografting pyridine molecules to an Ag electrode, additional capturing sites and favorable binding interactions were created, contributing to an increase in overall catalytic performance. We have shown that electrografted pyridine compounds enhance the stability of the key carboxyl intermediate (*COOH) and thereby lower the reaction energy barrier for the rate determining step and facilitate the CO_2RR. Two considerations contributed to the adoption of pyridine as a promoter: (i) chemically anchoring pyridines groups on the electrode surface through diazonium chemistry, can provide an opportunity for the nitrogen atom to be coordinated with *COOH; (ii) use of heterogeneous media requires smaller molecular loading to achieve the desired catalytic effect. The former modulates the electronic structure of the active Ag sites through an optimum charge delocalization for Ag-EPy-2, Ag-EPy-1, and Ag-EPy-3, respectively.

Conclusion

In summary, simple, and inexpensive pyridine molecules were shown to efficiently catalyze the electroreduction of CO_2 to C1 products with high selectivity and current density at low potential. Several pyridines of varying alkyl chain lengths were studied in order to better understand the synergistic effect between the catalyst structure and the surface electrode. Combined we demonstrated catalytic advantages greater than that of the individual catalyst structures, with a reduction in onset potential allowing for improved selectivities in H-cell studies. We hope that the above approach demonstrates the potential for this strategy to be generalized for other transition metals, and with further intentionally-designed molecular catalysts to continue to improve the efficiency of CO_2RR systems

Methods

DFT calculation

DFT computations were performed using Vienna Ab initio Simulation Package (VASP)[64] and on Compute Canada clusters. In all computations we used the projected augmented wave (PAW) pseudopotentials and the general gradient approximation (GGA) of Perdew-Burke-Ernzerhof (PBE) as their exchange-correlational functionals.[65] A cut-off energy of 450 eV for the plane wave basis sets and a 2×2×1 Γ-centered Monkhorst-Pack mesh for the k-points sampling in the first Brillouin zone, with a first order Methfessel-Paxton smearing parameter σ of 0.1 eV ensured that the energy convergence criteria is better than 1 meV for a vacuum of 20 Å or greater. The self-consistent field (SCF) convergence criterion is set to 1×10^{-4} eV for electronic iteration and the ionic relaxation continued till the maximum force was less than 0.02 eV/Å that was updated by the conjugate gradient approach. Dipole corrections and spin polarization are implemented. DFT-D3 method with Becke-Jonson damping is performed for the van der Waals correction.

Reaction steps were simulated over Ag(111) facet, as the most stable crystalline orientation of Ag, made of 100 silver atoms in 4 layers where, two top layers were allowed to be relaxed and two bottom ones were fixed in their optimized position to represent the characteristics of the bulk silver atoms. Figures S21 and S22, include three different hybride catalysts that were optimized after the addition of pyridines to the surface of the silver. To calculate the reaction energy diagram, the proton-coupled-electron-transfer (PCET) scheme[45] was followed using the computational hydrogen electrode (CHE)[66] *COOH and *CO demonstrate adsorbed carboxyl and carbon monoxide intermediates, respectively, where * denotes the catalyst surface. Optimized structures and equations used to calculate the reaction energy diagram are provided in the supporting information (equation Seq1 to Seq7). The electrostatic charge density around each ion is calculated by the Bader charge analysis method.[67] VESTA software is used for the visualization.[68]

Reaction mechanism on Ag 111 facet (* stands for the catalyst and i* is equivalent with adsorbed i):

Step 1) $* + CO_2 + H^+ + e^- \rightarrow COOH*$

Step 2) $COOH^* + H^+ + e^- \rightarrow CO^* + H_2O$

Therefore, for each step, writing the energy balance, we will have:

$$\Delta E_{rxn,1} = E_{COOH*} - E_* - E_{CO_2} - E_{H^+} - E_{e^-}$$

$$\Delta E_{rxn,2} = E_{CO*} + E_{H_2O} - E_{COOH*} - E_{H^+} - E_{e^-}$$

Modeling by proton-coupled electron transfer (PCET), we'll have:

$$H^+ + e^- \rightarrow \frac{1}{2}H_2, \Delta E_{rxn} = \frac{1}{2}E_{H_2} - E_{H^+} - E_{e^-} = 0$$

Thus, we can substitute ($E_{H^+} + E_{e^-}$) by half of the E_{H_2}, eventuating in:

$$\Delta E_{rxn,1} = E_{COOH*} - E_* - E_{CO_2} - \frac{1}{2}E_{H_2} \text{ (Equation-1)}$$

$$\Delta E_{rxn,2} = E_{CO*} + E_{H_2O} - E_{COOH*} - \frac{1}{2}E_{H_2} \text{(Equation-2)}$$

Reagents and Chemicals

All reagents and solvents were of commercial reagent grade and were used without further purification, except where noted. Reagents not listed were purchased from Sigma-Aldrich. 4-(2-Aminomethyl) Pyridine (98%), 4-Methylpyridine (99%), 4-Propylpyridine, 4-Aminopyridine (98%), Potassium Ferricyanide (III) (99%) Sodium nitrite (97%), Silver nitrite (99%), and Deuterium oxide (D_2O), (> 99.8 %D), Potassium bicarbonate (99.7%) were purchased from Sigma-Aldrich Company. All aqueous solutions were prepared using Millipore water (18.2 M Ω cm). Glassy carbon surface was polished with 1, 0.3 and 0.05 μm alumina slurries, respectively. The electrodes were then ultrasonicated in acetone, ethanol, and water

Material and Characterizations

All the spectroscopy data for structural characterizations were obtained using the research facilities at Delft University of Technology. ^{1}H NMR chemical shifts (δ) were reported in ppm in Deuterium Oxide (D_2O). The NMR data processed in MestReNova software. The reduced products observed in the cathodic

compartment were periodically collected from the reaction headspace and tested by gas chromatography (GC). The concentration of gaseous products (CO and H_2) was obtained from GC and the average of 4 injections was used to calculate their faradaic efficiencies. The gas product from carbon dioxide (CO_2) electroreduction (CO, H_2) was analysed using chromatograph (InterScience PerkinElmer Clarus 680) coupled with two thermal conductivity detectors (TCD) and a flame ionization detector (FID), while the liquid product was analyzed using HPLC (Infinity 1260 II LC, Agilent Technologies. Hi-Plex H column (@ 50C) with VWD (@ 210 nm and 280 nm) and RID (@40 C). ^{1}H NMR was measured using Bruker 400 MHz, and was processed in MestreNova and chemical shifts (δ) were reported in ppm.

X-ray photoemission spectroscopy (XPS) measurements were performed with a Thermo Scientific K-alpha spectrometer using a monochromatic Al Kα excitation source. The spectrometer was calibrated using the C 1s adventitious carbon with a binding energy of 284.8 eV. The base pressure at the analysis chamber was about $2 \cdot 10^{-9}$ mbar. The spectra were recorded using a spot size of 400 μm at pass energy of 50 eV and step size of 0.1 eV. Scanning electron microscopy (SEM) measurements were carried out with a FEI NovaNano SEM using secondary electron imaging with immersion lens mode and a 5 kV electron acceleration voltage.

Atomic force microscopy (AFM) was applied to characterize the surface microstructure of the silver catalyst layer of the gas-diffusion electrode. The Bruker's Dimension Icon equipped with TESPA-V2 tip performed the AFM characterization in a soft tapping mode. The height sensor and peak force error images of the catalyst layer were obtained during the test, and the 3D images were constructed based on the high sensor data by the NanoScope Analysis software.

Preparation of the Gas Diffusion Electrode

Ag-GDEs were made by magnetron sputtering (AJA International Inc.) Ag, MaTeck Germany, 99,9% purity) onto Freudenberg H14C10 GDL (Fuel Cell Store) to obtain a thin-film of Ag with 10 nm and 100 nominal thickness. During sputtering, the power supply was kept at 50 W DC with an Ar flow at 20 sccm (standard cubic centimeters per minute). The geometrical area of the GDL was 2.25 and 6.25 cm^2 for the

GDE-type and MEA-type flow cells, respectively. The electrode samples were kept in an Argon filled Glovebox prior to the electrografting and / or electrochemical testing.

Thin-film cathode preparation for ATR-SEIRAS

Thin-film cathodes were deposited on 60º Ge ATR crystals (Pike Technologies, 013-3132). These crystals were polished using alumina powder suspensions of decreasing grain-size (1.0µm, 0.3µm and 0.05µm) and then sonicated for 5 minutes in iso-propyl alcohol and deionized water. Before mounting in the DC magnetron sputtering setup, crystals were wiped with acetone using cotton swabs. Deposition of the Ag catalyst layer was performed in a magnetron sputtering system (PREVAC Project 229), at a chamber pressure of 25µbar, argon flowrate of 15sccm and power rate of 25W, for a deposition rate between 0.013 and 0.014nm/s and thickness of 40nm. Presence of the catalyst was confirmed both optically and by measuring the resistance over the film using a multimeter, which was between 3 and 4Ω. This procedure is strongly based to one reported in previous literature, but avoids air- or argon-plasma cleaning of the target while delivering comparable results.[50,69]

The electrochemical ATR-SEIRAS experiments were performed in a customized cell. The CO_2 reduction reaction occurs at the working electrode (WE) including Ag layer sputtered on top of the ATR crystal. A Pt counter electrode (CE), a Ag/AgCl reference electrode (RE), and a gas in- and outlet to purge CO_2. The electrolyte used was KCl due to its invisibility for infrared radiation, making it suitable for these measurements in order to isolate the intermediate species formed during CO_2 reduction on the catalyst surface. SEIRAS spectra were collected in a Brucker Vertex 70 modified FT-IR spectrometer, averaged over 72 scans at a resolution of $4cm^{-1}$. These spectra were collected as reflectance of the signal and transformed to absorbance units (a.u.) using the relation: $A = -\log(R/R_0)$. The sample chamber accommodates the proprietary cell and an additional N_2 purge (Figure S29).

Electrochemical routines were performed using a BioLogic SP-200 potentiostat. Before any spectroscopic measurement, the cell was purged for 30 min. using 99.999% pure CO_2 gas. This purge was also active

during electrochemistry. Before starting SEIRAS experiments, the Ag thin film was activated by applying 6 cyclic voltammetries from +0.2V to -1.1V *vs* Ag/AgCl. After this, background scans were collected at -0.5V *vs* Ag/AgCl, and consecutive scans every 50mV during a linear sweep voltammetry at 2mV/s. At -1.9 V *vs* Ag/AgCl, the potential was held for 7 scans before being reversed to OCV at the same scan-rate. The ATR-SEIRAS measurements were performed starting at the potential of -0.5 *vs* Ag/AgCl and gradually increased to the potential of -1.9 V *vs* RHE. During the infrared measurements, the cell was connected to a potentiostat that supplied a fixed potential to the working electrode.

H-cell Electrochemical Measurements

Both glassy carbon and silver electrodes served as solid-based working electrodes individually for a systematic comparison. For each electrochemical reaction, the solution was saturated with either CO_2 or Ar and the rest of the experiment was done in a sealed condition. All the electrolysis was done under stirring conditions. The electrochemical studies were carried out using a CHI 660C potentiostat (CH Instruments, Austin, TX) with a three-electrode set up enclosed in Faraday cage. Glassy carbon and sliver nanotubes (Ag) (working electrode), Pt wire (auxiliary) and Ag/AgCl (reference electrode). The electrodes were connected to the cell via a Nafion membrane bridge. The CV measurements were applied with positive initial scan polarity, 5 second quiet and the scan rate of 0.1 V/s. All potentials were reported versus the Ag/AgCl reference electrode. Potentials were changed from Ag/AgCl (3 M KCl) to RHE ($E_{RHE}=E_{Ag/AgCl} + 0.059 \times pH + 0.210$).

The impedance measurements were from 0.1 Hz - 100 kHz frequency range with 10 second quit time with a sampling rate of 4 points per decade, AC amplitude 10 mV, bias potential 0.28 V. The impedance detection electrolyte was aqueous solution containing 200 mM KNO_3 and 2.5 mM mol L^{-1} $K_3[Fe(CN)_6]/K_4[Fe(CN)_6]$ (1:1) as electroactive probe. The GC was equipped with a packed Molecular Sieve 5A capillary column and a packed HaySep D column. Helium (99.999%) was used as the carrier gas. A helium ionization detector (HID) was used to quantify H_2 and CO concentrations.

MEA-cell Electrochemical Measurements

All experiments were performed in a 5 cm^2 area membrane electrode assembly (Dioxide materials) having a serpentine flow channel on both the anode and cathode endplates. Sigracet 38 BC gas diffusion layers (GDL) of 6.25 cm^2 area (2.5 cm x 2.5cm) was used as the porous transport layer. Ag catalyst layer was deposited on top of microporous layer of GDL by direct current magnetron sputtering to obtain a thickness of 10 nm. Nickel foam (3 cm x 3 cm) was used as the anode. Ag GDE and Ni foam (Recemat BV) were combined with an oversized 16 cm^2 (4cm x 4cm) Sustainion anion exchange membrane (X37-50 Grade RT) to assemble the MEA. An exchange MEA configuration using 1M KOH as the anolyte and humidified CO_2 as reactant at the cathode were fed into the reactor at a flow rate of 50 sccm.

The MEA was prepared by physical compression of the electrodes and endplates using a torque wrench which were tightened to 4 Nm. This value was chosen to enhance the contact between the GDE and membrane while simultaneously ensuring that no physical damage occurred to the carbon GDE. A series of constant current electrolysis experiments were performed and the gaseous products from the cell were analysed using an online gas chromatography connected to the outlet of the cell equipped with two thermal conductivity detectors and a flame ionization detector. Constant current electrolysis from 10 mA/cm^2 to 200 mA/cm^2 was performed for 1200 seconds at each current density. Aliquots were collected every 5 min during the reaction resulting in a total of 4 injections for each current density in 1200 seconds.

The flow rate at the outlet of the reactor was measured using a mass flow meter (Bronkhorst) in order to estimate the faradaic efficiency of products accurately. A LABVIEW program was built and connected to the mass flow meter for continuous monitoring of the outlet flowrate. The outlet flow rate of the gas mixture (CO+H_2 +residual CO_2) from the reactor was measured ($\dot{V}_{outlet}$) using the mass flow meter and the mole fractions of CO (x_{CO}) and H_2 (x_{H_2}) were estimated from the GC injections.

Flow-cell Electrochemical Measurements

A flow cell with three compartments composed of gas, catholyte and anolyte chambers was used as reported from our group previously.[63] CO_2 was fed through a mass controller (Bronkhorst High-Tech BV) at a flow rate of 20 sccm. In all experiments the catholyte (100 mL) and anolyte (100 mL) were 1 M $KHCO_3$ (99.9% Sigma), supplied by a peristaltic pump at a rate of 20 mL/min. Nafion 115 proton exchange membrane was used to separate catholyte and anolyte. The electrochemically reacted gas and catholyte were sent into a gas-tight reservoir to balance the pressure at the gas and catholyte interface. Subsequently, gas was sent to GC for product analysis, while catholyte circulated back to catholyte chamber. Anolyte circulated through a different reservoir, which was open to atmosphere to allow anodic product O_2 to escape. The pH of electrolytes was measured before and after each test using a pH meter (HANNA, HI-98191).

Faradaic efficiency calculation

To estimate the Faradaic efficiency of gaseous products, the mole fractions of CO and H_2 were estimated from GC injections. The volume fraction of gas products from GC is equal to the mole fraction for ideal gases. The mole fraction of water vapour exiting the reactor was measured using a humidity sensor and found to be 78% (x_{H2O} = 0.023). Since the sum of mole fractions is equal to 1, the mole fraction of CO_2 exiting was calculated as Eq. S4.

Eq. S4:

$$x_{CO2,out} = 1 - (x_{CO} + x_{H2O} + x_{H2})$$

After calculating the mole fractions of all gaseous products, the volumetric flow rate at the outlet of the reactor measured with the MFM and used to calculate the moles of each product.

Eq. S5:

$$n_{CO} = \dot{V}_{outlet} \times x_{CO}$$

Eq. S6:

$$n_{H2} = \dot{V}_{outlet} \times x_{H2}$$

Eq. S7:

$$FE_{CO} = \frac{n_{CO} \times n^e \times F}{I} \times 100\ \%$$

Here: n_{CO} – moles/s of CO produced, n^e- number of electrons involved in CO_2RR (2 for CO), F- 96485 C/mol and I - applied current (in Amperes).

References

1. Davis, S. J., Caldeira, K. & Matthews, H. D. Future CO₂ Emissions and Climate Change from Existing Energy Infrastructure. *Science (80-.).* **329**, 1330 LP – 1333 (2010).

2. Yan, Z., Hitt, J. L., Turner, J. A. & Mallouk, T. E. Renewable electricity storage using electrolysis. *Proc. Natl. Acad. Sci.* **117**, 12558 LP – 12563 (2020).

3. Song, J. *et al.* Synthesis and Biochemical Evaluation of Thiochromanone Thiosemicarbazone Analogues as Inhibitors of Cathepsin L. *ACS Med. Chem. Lett.* **3**, 450–453 (2012).

4. Franco, F., Rettenmaier, C., Jeon, H. S. & Roldan Cuenya, B. Transition metal-based catalysts for the electrochemical CO2 reduction: from atoms and molecules to nanostructured materials. *Chem. Soc. Rev.* **49**, 6884–6946 (2020).

5. Boutin, E. *et al.* Molecular catalysis of CO2 reduction: recent advances and perspectives in electrochemical and light-driven processes with selected Fe, Ni and Co aza macrocyclic and polypyridine complexes. *Chem. Soc. Rev.* **49**, 5772–5809 (2020).

6. Abdinejad, M., Hossain, M. N. & Kraatz, H.-B. Homogeneous and heterogeneous molecular catalysts for electrochemical reduction of carbon dioxide. *RSC Adv.* **10**, 38013–38023 (2020).

7. Ting, L. R. L. *et al.* Enhancing CO2 Electroreduction to Ethanol on Copper–Silver Composites by Opening an Alternative Catalytic Pathway. *ACS Catal.* **10**, 4059–4069 (2020).

8. Monteiro, M. C. O. *et al.* Absence of CO2 electroreduction on copper, gold and silver electrodes

without metal cations in solution. *Nat. Catal.* **4**, 654–662 (2021).

9. Wang, J. *et al.* Silver/Copper Interface for Relay Electroreduction of Carbon Dioxide to Ethylene. *ACS Appl. Mater. Interfaces* **11**, 2763–2767 (2019).

10. Usman, M. *et al.* Electrochemical Reduction of CO2: A Review of Cobalt Based Catalysts for Carbon Dioxide Conversion to Fuels. *Nanomaterials* vol. 11 (2021).

11. Manbeck, G. F. & Fujita, E. A review of iron and cobalt porphyrins, phthalocyanines and related complexes for electrochemical and photochemical reduction of carbon dioxide. *J. Porphyr. Phthalocyanines* **19**, 45–64 (2015).

12. Bullock, R. M., Das, A. K. & Appel, A. M. Surface Immobilization of Molecular Electrocatalysts for Energy Conversion. *Chem. – A Eur. J.* **23**, 7626–7641 (2017).

13. Ma, Z. *et al.* Enhancing CO2 Electroreduction with Au/Pyridine/Carbon Nanotubes Hybrid Structures. *ChemSusChem* **12**, 1724–1731 (2019).

14. Marianov, A. N. & Jiang, Y. Covalent ligation of Co molecular catalyst to carbon cloth for efficient electroreduction of CO2 in water. *Appl. Catal. B Environ.* **244**, 881–888 (2019).

15. Luo, X. *et al.* Significant improvements in CO2 capture by pyridine-containing anion-functionalized ionic liquids through multiple-site cooperative interactions. *Angew. Chemie - Int. Ed.* **53**, 7053–7057 (2014).

16. Seshadri, G., Lin, C. & Bocarsly, A. B. A new homogeneous electrocatalyst for the reduction of carbon dioxide to methanol at low overpotential. *J. Electroanal. Chem.* **372**, 145–150 (1994).

17. Barton Cole, E. *et al.* Using a one-electron shuttle for the multielectron reduction of CO 2 to methanol: Kinetic, mechanistic, and structural insights. *J. Am. Chem. Soc.* **132**, 11539–11551 (2010).

18. Lim, C. H., Holder, A. M. & Musgrave, C. B. Mechanism of homogeneous reduction of CO2 by pyridine: Proton relay in aqueous solvent and aromatic stabilization. *J. Am. Chem. Soc.* **135**, 142–154 (2013).

19. Lim, C. H., Holder, A. M., Hynes, J. T. & Musgrave, C. B. Reduction of CO2 to methanol catalyzed by a biomimetic organo-hydride produced from pyridine. *J. Am. Chem. Soc.* **136**, 16081–16095 (2014).

20. Costentin, C., Canales, J. C., Haddou, B. & Savéant, J. M. Electrochemistry of acids on platinum. Application to the reduction of carbon dioxide in the presence of pyridinium ion in water. *J. Am. Chem. Soc.* **135**, 17671–17674 (2013).

21. Mattiuzzi, A. *et al.* Electrografting of calix[4]arenediazonium salts to form versatile robust platforms for spatially controlled surface functionalization. *Nat. Commun.* **3**, 1130 (2012).

22. Abdinejad, M., Santos da Silva, I. & Kraatz, H. B. Electrografting amines onto silver nanoparticle-modified electrodes for electroreduction of CO2 at low overpotential. *J. Mater. Chem. A* **9**, 9791–9797 (2021).

23. Abdinejad, M. *et al.* Enhanced Electrochemical Reduction of CO2 to CO upon Immobilization onto Carbon Nanotubes Using an Iron-Porphyrin Dimer. *ChemistrySelect* **5**, 979–984 (2020).

24. Baranton, S. & Bélanger, D. Electrochemical Derivatization of Carbon Surface by Reduction of in Situ Generated Diazonium Cations. *J. Phys. Chem. B* **109**, 24401–24410 (2005).

25. Andrieux, C. P. & Pinson, J. The Standard Redox Potential of the Phenyl Radical/Anion Couple. *J. Am. Chem. Soc.* **125**, 14801–14806 (2003).

26. Lyskawa, J. & Bélanger, D. Direct Modification of a Gold Electrode with Aminophenyl Groups by Electrochemical Reduction of in Situ Generated Aminophenyl Monodiazonium Cations. *Chem. Mater.* **18**, 4755–4763 (2006).

27. Üstündağ, Z. & Solak, A. O. EDTA modified glassy carbon electrode: Preparation and characterization. *Electrochim. Acta* **54**, 6426–6432 (2009).

28. Phal, S. *et al.* Electrografting of 4-Carboxybenzenediazonium on Glassy Carbon Electrode: The Effect of Concentration on the Formation of Mono and Multilayers. *Molecules* vol. 25 (2020).

29. Zhang, X. & Jiang, J. X-ray photoelectron spectroscopy of metal free porphyrazine, phthalocyanine and naphthalocyanine: density functional calculations. *J. Electron Spectros. Relat. Phenomena* **142**, 145–149 (2005).

30. Mou, Y. *et al.* Facile preparation of stable reactive silver ink for highly conductive and flexible electrodes. *Appl. Surf. Sci.* **475**, 75–82 (2019).

31. Gillan, L., Teerinen, T., Johansson, L.-S. & Smolander, M. Controlled diazonium electrodeposition towards a biosensor for C-reactive protein. *Sensors Int.* **2**, 100060 (2021).

32. Güzel, R., Ekşi, H., Üstündağ, Z. & Solak, A. O. Synthesis, characterization, and application of silver nanoparticle-thiophenol nanocomposite film on the glassy carbon surface. *Surf. Interface Anal.* **45**, 1821–1829 (2013).

33. Han, S. W., Kim, Y. & Kim, K. Dodecanethiol-Derivatized Au/Ag Bimetallic Nanoparticles: TEM, UV/VIS, XPS, and FTIR Analysis. *J. Colloid Interface Sci.* **208**, 272–278 (1998).

34. Peng, Z., Jiang, Z., Huang, X. & Li, Y. A novel electrochemical sensor of tryptophan based on silver nanoparticles/metal–organic framework composite modified glassy carbon electrode. *RSC Adv.* **6**, 13742–13748 (2016).

35. Abdinejad, M., Dao, C., Zhang, X. & Kraatz, H. B. Enhanced electrocatalytic activity of iron amino porphyrins using a flow cell for reduction of CO2 to CO. *J. Energy Chem.* **58**, 162–169 (2021).

36. Ma, S., Lan, Y., Perez, G. M. J., Moniri, S. & Kenis, P. J. A. Silver Supported on Titania as an

Active Catalyst for Electrochemical Carbon Dioxide Reduction. *ChemSusChem* **7**, 866–874 (2014).

37. Electron Transfer, Bond Breaking, and Bond Formation. *Elements of Molecular and Biomolecular Electrochemistry* 182–250 (2006) doi:https://doi.org/10.1002/0471758078.ch3.

38. Shafaei Douk, A., Saravani, H., Yazdan Abad, M. Z. & Noroozifar, M. Three-Dimensional Engineering of Nanoparticles To Fabricate a Pd–Au Aerogel as an Advanced Supportless Electrocatalyst for Low-Temperature Direct Ethanol Fuel Cells. *ACS Appl. Energy Mater.* **3**, 7527–7534 (2020).

39. Ngamchuea, K., Eloul, S., Tschulik, K. & Compton, R. G. Planar diffusion to macro disc electrodes—what electrode size is required for the Cottrell and Randles-Sevcik equations to apply quantitatively? *J. Solid State Electrochem.* **18**, 3251–3257 (2014).

40. Mishyn, V. *et al.* "Click" Chemistry on Gold Electrodes Modified with Reduced Graphene Oxide by Electrophoretic Deposition. *Surfaces* vol. 2 (2019).

41. Gabardo, C. M. *et al.* Combined high alkalinity and pressurization enable efficient CO2electroreduction to CO. *Energy Environ. Sci.* **11**, 2531–2539 (2018).

42. Rosen, B. a *et al.* Ionic Liquid – Mediated Selective Conversion of CO 2 to CO at Low Overpotentials. *Science (80-.).* **334**, 643–644 (2011).

43. Abdinejad, M., Mirza, Z., Zhang, X. & Kraatz, H.-B. Enhanced Electrocatalytic Activity of Primary Amines for CO2 Reduction Using Copper Electrodes in Aqueous Solution. *ACS Sustain. Chem. Eng.* **8**, 1715–1720 (2020).

44. Fernandes, D. M., Peixoto, A. F. & Freire, C. Nitrogen-doped metal-free carbon catalysts for (electro)chemical CO2 conversion and valorisation. *Dalt. Trans.* **48**, 13508–13528 (2019).

45. Huynh, M. H. V & Meyer, T. J. Proton-Coupled Electron Transfer. *Chem. Rev.* **107**, 5004–5064

(2007).

46. Zhu, S., Li, T., Cai, W.-B. & Shao, M. CO2 Electrochemical Reduction As Probed through Infrared Spectroscopy. *ACS Energy Lett.* **4**, 682–689 (2019).

47. Dunwell, M., Yan, Y. & Xu, B. In Situ Infrared Spectroscopic Investigations of Pyridine-Mediated CO2 Reduction on Pt Electrocatalysts. *ACS Catal.* **7**, 5410–5419 (2017).

48. Smith, E. L. & Porter, M. D. Structure of monolayers of short chain n-alkanoic acids (CH3(CH2)nCOOH, n = 0-9) spontaneously adsorbed from the gas phase at silver as probed by infrared reflection spectroscopy. *J. Phys. Chem.* **97**, 8032–8038 (1993).

49. Lee, S. J., Han, S. W., Yoon, M. & Kim, K. Adsorption characteristics of 4-dimethylaminobenzoic acid on silver and titania: diffuse reflectance infrared Fourier transform spectroscopy study. *Vib. Spectrosc.* **24**, 265–275 (2000).

50. Firet, N. J. & Smith, W. A. Probing the Reaction Mechanism of CO2 Electroreduction over Ag Films via Operando Infrared Spectroscopy. *ACS Catal.* **7**, 606–612 (2017).

51. Baruch, M. F., Pander, J. E., White, J. L. & Bocarsly, A. B. Mechanistic Insights into the Reduction of CO2 on Tin Electrodes using in Situ ATR-IR Spectroscopy. *ACS Catal.* **5**, 3148–3156 (2015).

52. Lambert, D. K. Vibrational Stark effect of adsorbates at electrochemical interfaces. *Electrochim. Acta* **41**, 623–630 (1996).

53. Wang, C., Luo, H., Jiang, D., Li, H. & Dai, S. Carbon Dioxide Capture by Superbase-Derived Protic Ionic Liquids. *Angew. Chemie Int. Ed.* **49**, 5978–5981 (2010).

54. Abdinejad, M. *et al.* Electrocatalytic Reduction of CO2 to CH4 and CO in Aqueous Solution Using Pyridine-Porphyrins Immobilized onto Carbon Nanotubes. *ACS Sustain. Chem. Eng.* **8**, 9549–9557 (2020).

625 55. Dinh, C. T. *et al.* CO2electroreduction to ethylene via hydroxide-mediated copper catalysis at an
626 abrupt interface. *Science (80-.).* **360**, 783–787 (2018).

627 56. Pang, Y. *et al.* Joint tuning of nanostructured Cu-oxide morphology and local electrolyte programs
628 high-rate CO2 reduction to C2H4. *Green Chem.* **19**, 4023–4030 (2017).

629 57. Weekes, D. M., Salvatore, D. A., Reyes, A., Huang, A. & Berlinguette, C. P. Electrolytic CO2
630 Reduction in a Flow Cell. *Acc. Chem. Res.* **51**, 910–918 (2018).

631 58. Jouny, M., Luc, W. & Jiao, F. High-rate electroreduction of carbon monoxide to multi-carbon
632 products. *Nat. Catal.* **1**, 748–755 (2018).

633 59. Lin, K. *et al.* Alkaline quinone flow battery. *Science (80-.).* **349**, 1529 LP – 1532 (2015).

634 60. Dinh, C.-T., Li, Y. C. & Sargent, E. H. Boosting the Single-Pass Conversion for Renewable
635 Chemical Electrosynthesis. *Joule* **3**, 13–15 (2019).

636 61. Lee, S. *et al.* Sustainable production of formic acid by electrolytic reduction of gaseous carbon
637 dioxide. *J. Mater. Chem. A* **3**, 3029–3034 (2015).

638 62. Subramanian, S., Middelkoop, J. & Burdyny, T. Spatial reactant distribution in CO2 electrolysis:
639 balancing CO2 utilization and faradaic efficiency. *Sustain. Energy Fuels* **5**, 6040–6048 (2021).

640 63. Liu, K., Smith, W. A. & Burdyny, T. Introductory Guide to Assembling and Operating Gas
641 Diffusion Electrodes for Electrochemical CO2 Reduction. *ACS Energy Lett.* **4**, 639–643 (2019).

642 64. Kresse, G. & Hafner, J. Ab initio molecular dynamics for liquid metals. *Phys. Rev. B* **47**, 558–561
643 (1993).

644 65. Perdew, J. P., Burke, K. & Ernzerhof, M. Generalized Gradient Approximation Made Simple.
645 *Phys. Rev. Lett.* **77**, 3865–3868 (1996).

646 66. Nørskov, J. K. *et al.* Origin of the Overpotential for Oxygen Reduction at a Fuel-Cell Cathode. *J.*

Phys. Chem. B **108**, 17886–17892 (2004).

67. Tang, W., Sanville, E. & Henkelman, G. A grid-based Bader analysis algorithm without lattice bias. *J. Phys. Condens. Matter* **21**, 84204 (2009).

68. Momma, K. & Izumi, F. VESTA: a three-dimensional visualization system for electronic and structural analysis. *J. Appl. Crystallogr.* **41**, 653–658 (2008).

69. Corson, E. R. *et al.* In Situ ATR-SEIRAS of Carbon Dioxide Reduction at a Plasmonic Silver Cathode. *J. Am. Chem. Soc.* **142**, 11750–11762 (2020).

Acknowledgements (optional)

Ali Seifitokaldani acknowledges NSERC for its Discovery Grant (RGPIN-2020-04960), Canada Research Chair (950-23288) and FRQNT New Researchers Fund (2021-NC-283234) to support this study. Computations in this research were enabled in part by support provided by Calcul Quebec and Compute Canada.

Ethics declarations

All authors have given approval to the final version of the manuscript.

Supplementary Files

This is a list of supplementary files associated with this preprint. Click to download.

- SupportingInformation.pdf